J Mater Sci (2017) 52:4070–4085

Grain boundary character distribution in electroplated nanotwinned copper

Sutatch Ratanaphan[1,*], Dierk Raabe[2,*], Rajchawit Sarochawikasit[3], David L. Olmsted[4], Gregory S. Rohrer[5], and K. N. Tu[6]

[1] *Department of Tool and Materials Engineering, King Mongkut's University of Technology Thonburi, 126 Pracha Uthit Rd, Thung Khru, Bangkok 10140, Thailand*
[2] *Max-Planck-Institut für Eisenforschung, Max-Planck-Str. 1, 40237 Düsseldorf, Germany*
[3] *Department of Computer Engineering, King Mongkut's University of Technology Thonburi, 126 Pracha Uthit Rd, Thung Khru, Bangkok 10140, Thailand*
[4] *Department of Materials Science and Engineering, University of California, Berkeley, CA 94720-1760, USA*
[5] *Department of Materials Science and Engineering, Carnegie Mellon University, Pittsburgh, PA 15213-3890, USA*
[6] *Department of Materials Science and Engineering, University of California, Los Angeles, CA 90095-1595, USA*

Received: 1 November 2016
Accepted: 9 December 2016
Published online: 22 December 2016

ABSTRACT

The grain boundary character distribution (GBCD) of nanotwinned copper, fabricated by electroplating inside small-scale through-wafer vias, was characterized using a stereological interpretation of electron backscatter diffraction maps. The GBCD of electroplated nanotwinned copper, specified by five macroscopic parameters (three for the lattice misorientation and two for the grain boundary plane inclination), is similar to the GBCD of coarse-grained polycrystalline copper used here as a reference material. The GBCD was compared to calculated grain boundary energies determined from atomistic simulations. We find that the grain boundary population in the electroplated nanotwinned and coarse-grained reference copper is both on average inversely correlated to the grain boundary energies. The slopes of the relationships between grain boundary population and energy for the most highly populated misorientations (Σ3, Σ9, and Σ11) are different. The relationships are strongly influenced by the geometric constraints at the triple junctions and multiple twinning, which enhanced the observed frequencies of Σ9 boundaries. The results suggest that the grain boundary network and the GBCD in the polycrystalline specimens are strongly influenced by the microstructure, grain boundary energy, and multiple twining.

Address correspondence to E-mail: sutatch.ratanaphan@mail.kmutt.ac.th; d.raabe@mpie.de

DOI 10.1007/s10853-016-0670-5

Introduction

Most solid materials are polycrystalline, meaning that they consist of multiple crystals (grains) and a network of internal interfaces where the grains abut (grain boundaries). The geometric structure of the grain boundary is crystallographically defined by five macroscopic degrees of freedom (three for a lattice misorientation and two for a grain boundary plane orientation [1–3]. It has been well established that increasing the population of special boundaries can significantly affect and actually improve a wide range of material properties [4, 5]. For example, mechanical strength, electrical conductivity, segregation, damage, and corrosion resistance are strongly correlated to the fraction of special grain boundaries in polycrystalline materials [4–16]. These special grain boundaries, which are often characterized by superior properties compared to average boundaries, have low energies and are terminated by at least one low index plane [16–21]. Processing methods used to increase and utilize the occurrence of special grain boundaries are referred to as Grain Boundary Engineering (GBE) [21–26].

The most common practice is to use thermo-mechanical processing to enhance the frequency of Σ3 boundaries in polycrystalline materials [13, 25–34]. This technique can only be used for coarse-grained polycrystalline materials due to the substantial grain growth during thermal annealing. Recently, it was reported that nanotwinned polycrystalline copper synthesized by electroplating [8, 9, 35–37] and magnetron sputtering techniques [10, 38] exhibits high hardness, high resistance to electromigration, and yet normal electrical conductivity comparable to that of pure copper. These observations represent a paradigm shift for grain boundary engineering (GBE), making it possible to tailor nano-polycrystalline materials with an increased fraction of desired grain boundaries. Nevertheless, only a few studies investigated the grain boundary character distribution (GBCD) of nanotwinned copper [8, 9]. Previous studies examined the microstructure of nanotwinned copper using transmission electron microscopy (TEM) [8–10, 39]; however, the results of these studies do not provide enough data to quantify the population distribution of grain boundaries over all five parameters. Therefore, the objective of the present study is to investigate the GBCD in nanotwinned copper using electron backscatter diffraction (EBSD), which has a wider field of view than TEM [39–42].

A second objective of the study is to compare the GBCD of nanotwinned copper to the GBCD of coarse-grained reference copper. In coarse-grained polycrystalline materials, it is known that grain boundary populations are, on average, inversely correlated to the grain boundary energy distribution (GBED) [43–48]. While the grain boundary population in nanocrystalline tungsten is also inversely correlated to the grain boundary energy [49, 50], this may or may not be true for electroplated nanotwinned copper. The relationship between the GBCD and GBED is thought to be established during grain growth [51, 52], and nanostructured materials formed by electroplating undergo much less grain growth than in a coarse-grained material. Whether or not sufficient grain growth occurs in a nanocrystalline material to establish the same GBCD as a coarse-grained microstructure with the same chemical composition is not known. Therefore, the main purpose of the present study is to determine whether or not the GBCD of electroplated nanotwinned copper is inversely correlated to the GBED. We therefore compare the GBCD of electroplated nanotwinned copper to the GBCD of high-purity coarse-grained copper, and grain boundary energies extrapolated from simulated grain boundary energies [53] using the function established by Bulatov et al. [54]. It is expected that the relationships between grain boundary structure, energy, and population in nanotwinned copper will lead to a better understanding of the formation mechanism of coherent twin boundaries in nanotwinned copper.

Experimental procedures

The nanotwinned copper was plated from a copper electrolyte composed of copper sulfate, sulfuric acid, hydrochloric acid, and organic additives (ATOTECH, Germany) [55]. The plating conditions are similar to a pulsed plating condition with a pulse on-time of 20 ms and a pulse off-time of 1 ms. However, to deposit copper into high-aspect ratio through-wafer vias with a diameter of 100 μm, the current densities and pulse conditions were varied with thickness. Specifically, low forward current densities (10–25 mA/cm^2) and high reverse current density (65–45 mA/cm^2) were used during the pulse on- and off-times, respectively [9]. The details of the electroplating technique were reported elsewhere [9, 55].

The coarse-grained copper specimens were prepared from cold rolled copper sheets, Alfa Aesar Puratronic (99.9999%), which were annealed in a hydrogen flow furnace at 300 °C for 2 h. The surfaces of the coarse-grained copper were prepared by grinding with SiC papers (400, 600, 800, and 1200 grits), polishing with a diamond paste (3 μm), and fine polishing with colloid silica (40 nm). For the nanotwinned copper samples, surface deformation from mechanical polishing was removed by argon ion milling (Gatan 1682, 2 keV for 15 min).

The crystal orientations of the copper specimens were characterized using a high-resolution field emission scanning electron microscope equipped with an electron backscatter diffraction (EBSD) detector. The specimens were tilted at an angle of 70°. The measurements were carried out using a 15 keV electron beam and a working distance of 15 mm. Regular hexagonal grids with a step size of 100 nm and 1 μm were used for the nanotwinned copper and coarse-grained copper, respectively. To remove misindexed data from the measurement, the crystal orientation maps were processed by standard clean-up routines using the TSL OIM software. The raw data were first processed using a neighbor confidence index (CI) correction, in which the crystal orientation and the CI of all pixels with CI < 0.1 were changed to the ones of the neighbor pixels having the highest CI. The confidence indices of all points in a grain were then changed to the highest CI found in the grain using a grain CI standardization. The data were subsequently processed with grain dilation using a single step with a minimum grain size of 50 pixels and a tolerance angle of 5°. Finally, the crystallographic orientation of the grain was determined from the average orientation of all pixels within the grain. The reconstructed grain boundary line segments used for the stereological GBCD calculation were extracted from the processed EBSD maps. When line segments deviated from the grain boundary plane were more than two pixels, the segments were divided to obtain a better match with the curvatures of grain boundaries [56]. The GBCDs of nanotwinned and coarse-grained copper were calculated from 51,771 and 51,777 line segments using the stereological method with a texture correction scheme and a binning resolution of 10° [1, 2, 6]. The technique is described in detail elsewhere [57]. The GBCDs are measured in multiples of a random distribution (MRD). Values greater than one indicate that the boundaries are observed more frequently than expected in a random distribution.

To investigate the relationship between grain boundary population and energy, we compare the grain boundary population to the grain boundary energy of copper derived from the grain boundary energy function for FCC metals proposed by Bulatov et al. [54]. The function provides a method of

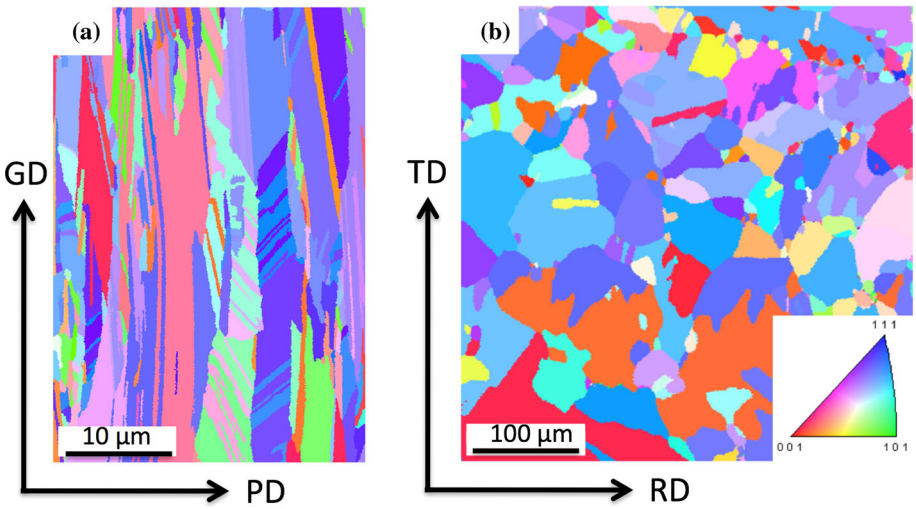

Figure 1 EBSD maps of the electroplated nanotwinned copper (**a**) and coarse-grained copper (**b**). The *inset* in **b** indicates the crystallographic vectors used to color orientations in the maps. The electroplated nanotwinned image is colored with reference to growth direction (GD) and in plane direction (PD). For the coarse-grained copper, the rolling direction (RD) is perpendicular to transverse direction (TD) and normal direction (ND). Note that the *scale bar* in the nanotwinned copper is ten times smaller than that in the coarse-grained copper. These are representative subsets of all the data.

extrapolating between known points established by embedded-atom method simulations [53]. In this study, we use a catalog of the 39777 grain boundaries that can be constructed in a periodic cell with dimensions less than or equal to $55a_0/2$, where a_0 is the lattice spacing [58]. The construction of these grain boundaries was described in references [53, 59]. This catalog has 1058 different misorientations, and the largest Σ in the dataset is 34075. These boundaries are not evenly distributed across the five macroscopic degrees of freedom. There are 1429 Σ3, 934 Σ5, 611 Σ7, 984 Σ9, and 445 Σ11 boundaries.

Results

Representative EBSD maps of the specimens are shown in Fig. 1. There are multiple nanotwinned lamellae, which are elongated parallel to each other in the parental grain in the electroplated copper specimen as illustrated in Fig. 1a. The coarse-grained copper in Fig. 1b has equiaxed grains with curved boundaries. The sizes of the grains in the coarse-grained copper are much larger than those in the electroplated nanotwinned copper. The electroplated nanotwinned copper has a strong [110] fiber texture parallel to the growth direction as shown in Fig. 2a. The coarse-grained copper in Fig. 2b has (001) [100] cube texture, which is consistent with the annealing texture of cold rolled copper foils [60, 61]. The relative areas for grain boundary planes for all misorientations of the specimens are shown in the grain boundary plane distributions (GBPD) in Fig. 3. The GBPD of the electroplated nanotwinned copper (Fig. 3a) is similar to what is observed in the coarse-grained copper (Fig. 3b).

While the maxima in the grain boundary plane distributions for electroplated nanotwinned (Fig. 3a)

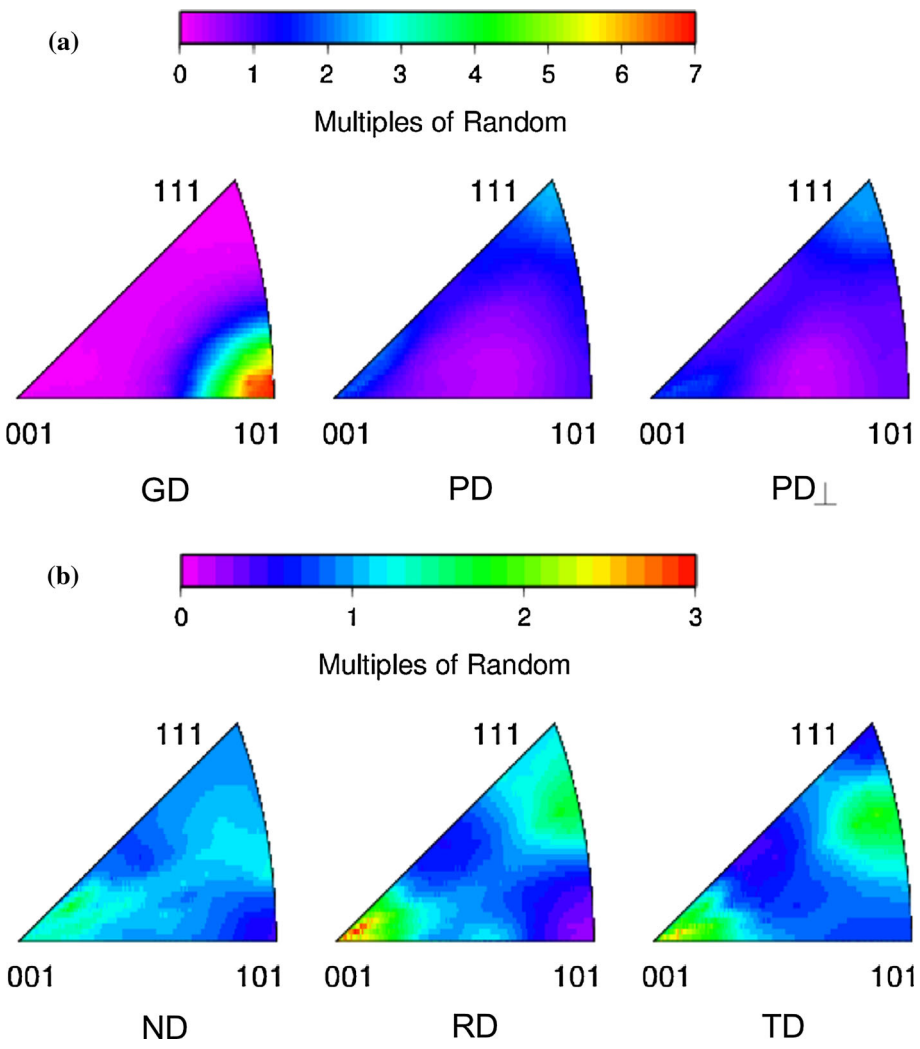

Figure 2 Inverse pole figures for the electroplated nanotwinned copper (**a**) and coarse-grained copper (**b**). The frequency of the crystallographic texture components is specified in units of multiples of a random distribution (MRD). Nanotwinned copper has a strong [101] fiber texture parallel to the growth direction (GD). Note that PD⊥ is the sample reference direction that is perpendicular to the [101] growth direction (GD) and in plane direction (PD). The distributions of coarse-grained copper are plotted with the reference direction parallel to the normal direction (ND), rolling direction (RD), and transverse direction (TD) of the sample.

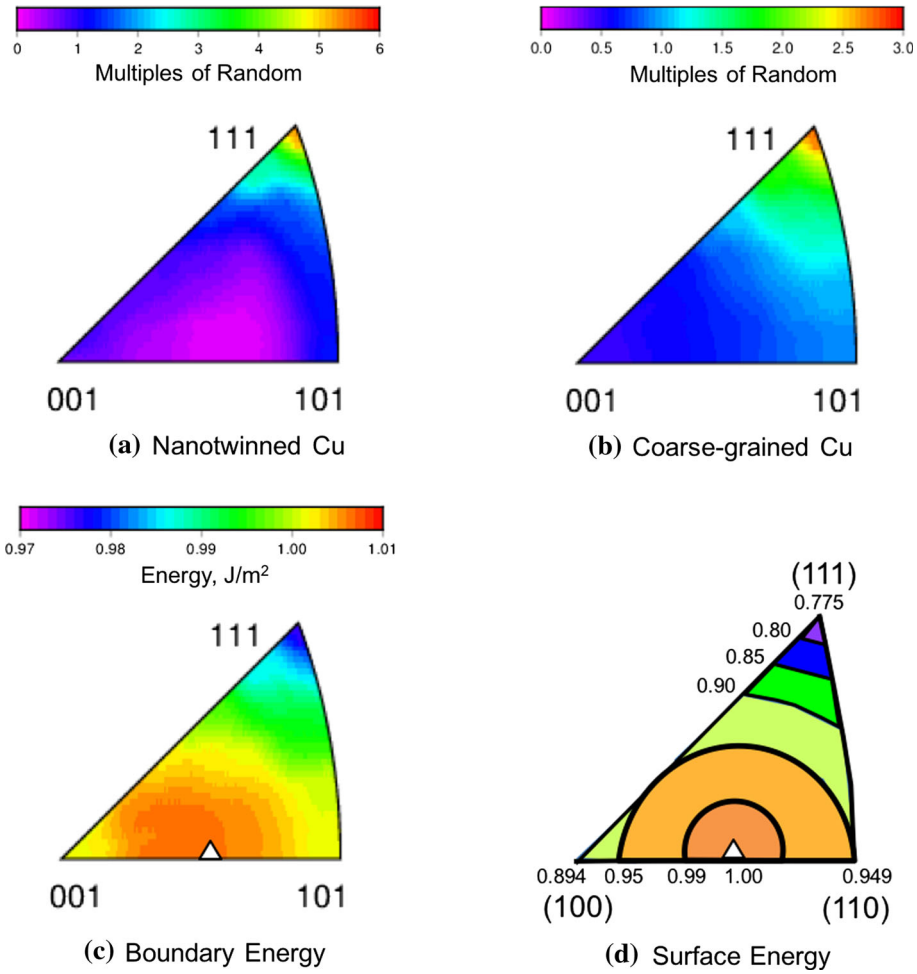

Figure 3 Grain boundary plane distributions (GBPD) calculated without considering the misorientation in the electroplated nanotwinned copper (**a**) and coarse-grained copper (**b**). The frequencies of the observed grain boundary planes are specified in the units of multiples of a random (MRD). The distribution of grain boundary energy in copper (**c**) is similar to the distribution of surface energy (**d**) calculated from the nearest neighbor broken bond model for FCC metals, reproduced from Ref. [62]. The units for energy are scaled with E (210) = 1.00 (energy maximum) represented as a *triangle* in the figure.

and coarse-grained copper (Fig. 3b) are both centered at the (111) position, the maximum in the nanotwinned copper (6.0 MRD) is much greater than that in the coarse-grained copper (2.9 MRD). The GBPD in the nanotwinned copper has its minimum (0.1 MRD) at the (210) position. The relative area for the (210) grain boundary plane in the coarse-grained copper (0.7 MRD) is slightly larger than the actual minimum value (0.5 MRD) at (001) position in Fig. 3b. The grain boundary energy distribution for copper, derived from the energies of 39777 grain boundaries extrapolated from the boundary energy function [54], is shown in Fig. 3c. The distribution is similar to the measured boundary energies in the FCC metals (nickel [44] and austenitic steel [48]) and the distribution of surface energy calculated from the nearest-neighbor broken-bond model (Fig. 3d) [62]. While the broken-bond model is not expected to be quantitatively accurate, it agrees well with the experimental results [63] and the results obtained from molecular dynamics simulations conducted in conjunction with an embedded-atom potential model [64]. The minimum and the maximum values in the grain boundary energy functions are similar to the distribution of the surface energy [62–64], which has the minimum and maximum at (111) and (210), respectively. This result implies that the energy of a grain boundary in Fig. 3c is correlated to the energy of the surfaces in Fig. 3d that makes up the grain boundary [4, 65].

The results of the average relationships between the grain boundary populations and the grain boundary energies are plotted in Fig. 4a. The grain boundary energies in copper are sorted into equal bins with 0.05 J/m^2 intervals. The average values of grain boundary energy in each bin are calculated, and the average populations for all grain boundaries in a given bin are then calculated. The analysis demonstrates that the grain boundary populations in the electroplated nanotwinned copper and in the coarse-grained copper are on the average correlated

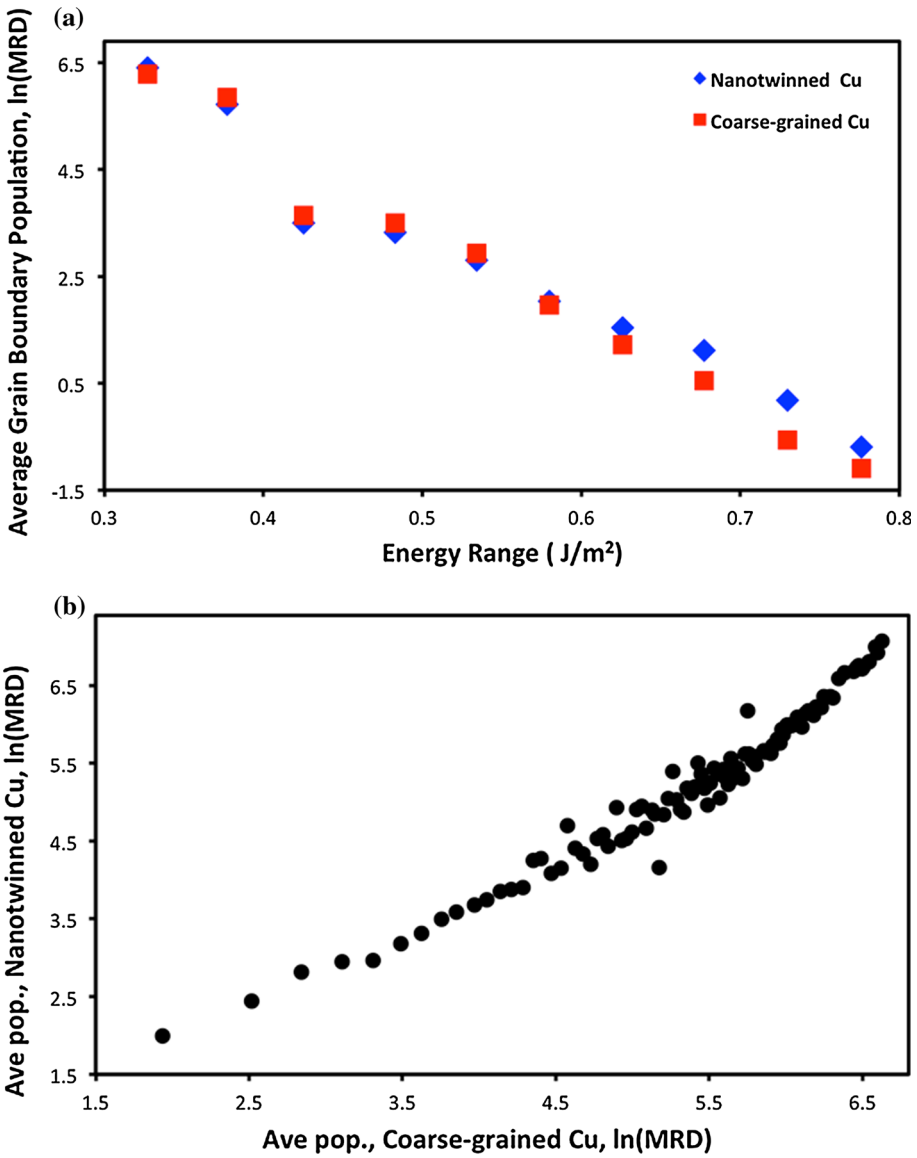

Figure 4 Average relationships between grain boundary populations and energies in the electroplated nanotwinned and the reference coarse-grained copper specimens (**a**). Comparison of average population (Ave pop.) in the electroplated nanotwinned and coarse-grained copper is shown in **b**. The populations and energies are classified into equally spaced bins with a width of 5 MRD and 0.05 J/m^2 respectively. Note that the populations are plotted using a logarithmic scale.

inversely to the grain boundary energy, which is consistent with the previously observed correlation in polycrystalline materials [43–48, 66]. The comparison between the average grain boundary populations in the two types of copper specimens is shown in Fig. 4b. The grain boundary populations in the coarse-grained copper are sorted into equal bins with an interval of 5 MRD; the average populations for the same grain boundaries in the electroplated nanotwinned copper are then calculated and used as the vertical coordinate. This result indicates a strong correlation and also suggests that, on average, the grain boundary population distributions in the copper specimens are mainly controlled by the grain boundary energy and that even in the electroplated specimen, there was enough grain growth to reach the same distribution as the coarse-grained specimen.

The fractional interface lengths, quantified using Brandon's criterion [67], for the Σ3, Σ9, Σ11, Σ27a, and Σ27b boundaries are 54% (60%), 0.9% (2.9%), 0.9% (0.11%), 0.2% (0.5%), and 0.01% (0.3%), respectively, in the electroplated nanotwinned copper (coarse-grained copper). While the fraction of all Σ3 boundaries in the electroplated nanotwinned copper (54%) is slightly lower than that in the coarse-grained copper (60%), the fraction of coherent twin

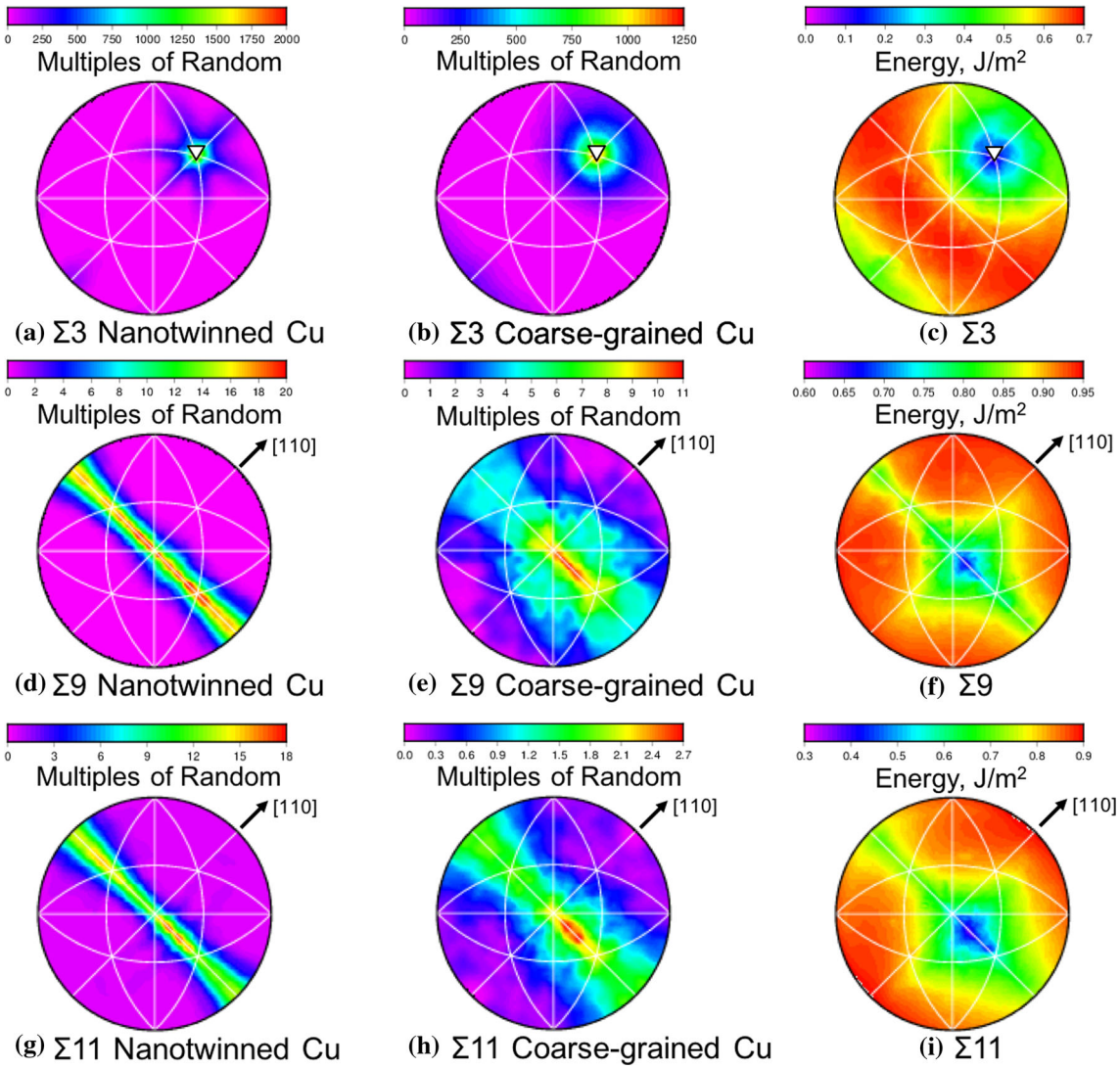

Figure 5 Grain boundary plane distributions for the electroplated nanotwinned copper (**a**, **d**, **g**) and the coarse-grained copper reference sample (**b**, **e**, **h**) plotted in stereographic projection with units of multiples of a random distribution (MRD). The distributions of grain boundary energy in copper for Σ3, Σ9, and Σ11 misorientations are derived from the grain boundary energy function [54] and plotted in **c**, **f**, and **i** respectively. The [100], [010], and [001] directions are pointing along the horizontal, vertical, and perpendicular to the page, respectively. In **a**–**c**, the [111] misorientation axis is marked by a *triangle*, the misorientation axes in the other misorientations are in the plane of the page and marked by the *arrows*.

boundaries in the electroplated nanotwinned copper (46%) is significantly higher than that in the coarse-grained copper sample (27%).

The grain boundary plane and energy distributions are plotted for the most commonly observed misorientations (Σ3 at 60° around [111], Σ9 at 38.9° around [110], and Σ11 at 50.5° around [110]) in Fig. 5. Note that the GBCD was calculated with discrete 10° bins, and, for this reason, the Σ27a boundary cannot be distinguished from the Σ9 boundary. The distributions are plotted as stereographic projections using the bicrystal reference frame. For the Σ3 misorientation, the population distributions in nanotwinned copper (Fig. 5a) and in coarse-grained copper (Fig. 5b) reveal a very strong peak at the (111) twist boundary orientation. While these two distributions have a similar shape in which the maximum is located at the lowest boundary energy (the coherent twin boundary, 0.02 J/m^2), the relative area for the coherent twin boundary in the electroplated nanotwinned copper (1800 MRD) is much greater than that in the coarse-grained copper (1200 MRD),

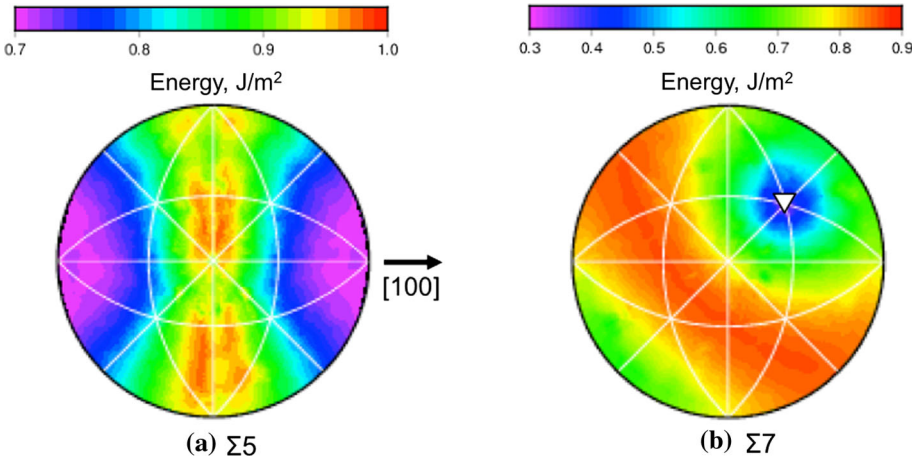

Figure 6 The distributions of the grain boundary energy in copper for Σ5 and Σ7 misorientations are derived from the grain boundary energy function [54] and plotted in **a**, **b**, respectively. The [100], [010], and [001] directions are pointing along the horizontal, vertical, and perpendicular to the page, respectively. For Σ5, the [100] misorientation axe is in the plane of the page and marked by the *arrows*. For Σ7, the [111] misorientation axis is marked by a *triangle*.

consistent with the higher concentration of coherent twin boundaries, noted above. The relative areas for grain boundaries at the Σ9 misorientation in the electroplated nanotwinned copper and in the coarse-grained copper have the maxima along the [110] zone, as shown in Fig. 5d, e, respectively. Because the maximum extends across many grain boundary plane orientations, there are combinations of asymmetric and symmetric tilt grain boundaries.

While the maximum of the grain boundary population distribution for the coarse-grained copper at the Σ9 misorientation (11 MRD) is located at the (1–14) symmetric tilt boundary, the peak maximum in the nanotwinned copper (20 MRD) is located at the asymmetric tilt boundary with (16,13,13)/(8,1,1). It should be noted that the boundary energy of this asymmetric tilt boundary (0.74 J/m^2) is comparable to the energy of the (1–14) symmetric tilt boundary (0.61 J/m^2), which is the lowest grain boundary energy at the Σ9 misorientation in Fig. 5f. Grain boundary population distributions at the Σ11 misorientation in the electroplated nanotwinned copper and in the coarse-grained copper as illustrated in Fig. 5g, h, respectively, are similar to the distributions for the Σ9 misorientation. The grain boundary energy distribution at the Σ11 misorientation in Fig. 5i is also similar to the distribution at the Σ9 misorientation. The lowest boundary energy at the Σ11 misorientation is the (1–13) symmetric tilt boundary (0.31 J/m^2), which is significantly lower in energy than the boundary energy of the (1–14) symmetric tilt boundary (0.61 J/m^2) at the Σ9 misorientation. The boundary populations at the Σ9 and Σ11 misorientations in the electroplated nanotwinned copper are much more spread out along the [110] zone and greater than what is observed for the coarse-grained polycrystalline copper. The larger maxima in the electroplated nanotwinned copper are probably a direct result of the growth texture. With the dominant crystal orientation along [110], and the columnar grain shape, the grain boundary plane orientations are frequently perpendicular to [110], and this leads to the large population of [110] tilt boundaries.

The grain boundary energy distributions for the Σ5 and Σ7 boundaries are presented in Fig. 6. However, we observed so few of these boundaries in the specimens that the grain boundary plane distributions at these misorientations contribute so little significance to the overall distribution that we do not discuss them in more detail. The absence of Σ7 boundaries is unusual. The lowest energy Σ7 boundary (0.31 J/m^2) is comparable to the lowest energy Σ11 boundary (0.31 J/m^2) and almost half the lowest energy Σ9 boundary (0.61 J/m^2). Therefore, one would expect Σ7 boundaries to occur with approximately the same frequency as Σ11 boundaries and more than Σ9 boundaries, but this is not the case. In fact, the populations at the lowest energy Σ7 grain boundary, the (111) twist boundary, are only 0.25 and 0.4 MRD in the nanotwinned and coarse-grained copper, respectively.

Discussion

In this study, the relative grain boundary areas in polycrystalline copper specimens fabricated by the electrodeposition technique and by rolling plus thermal annealing are measured and compared to the grain boundary energy. The microstructure of electroplated copper is dominated by the parameters of the deposition method, while the coarse-grained copper is dominated by recrystallization and grain growth. We find that the microstructure and texture of the electroplated copper are very different from those observed for the coarse-grained copper. Specifically, the electroplated copper has multiple parallel twin plates and strong directional growth with [110] fiber texture, while the coarse-grained copper has a weak texture with equiaxed grains as shown in Figs. 1 and 2.

One of the most interesting results is the inverse relationship between the average grain boundary population and the average grain boundary energy in the electroplated and coarse-grained copper in Fig. 4a. While the average populations and the average energy in the electroplated nanotwinned and coarse-grained copper are inversely correlated, it is apparent that low boundary energies do not have high populations in every instance, as illustrated for the Σ7 boundary. Specifically, the (111) twist boundary at Σ7 (0.31 J/m^2), which is the lowest boundary energy at this misorientation, is less frequently observed than the (1–14) symmetric tilt boundary (0.61 J/m^2) at the Σ9 misorientation. To investigate the relationship between grain boundary population and grain boundary energy for individual boundaries, the grain boundary populations of the most highly populated grain boundaries (Σ3, Σ9, and Σ11 misorientations) are plotted together with the grain boundary energies in Fig. 7. Comparisons between grain boundary population and energy for these misorientations (on a boundary-by-boundary basis) in the electroplated nanotwinned copper as shown in Fig. 7a indicate significant scatter and a weak correlation. The grain boundary network in the electroplated film does not reach the same distribution as in the coarse-grained copper that reveals a much stronger inverse correlation with the grain boundary energy, as shown in Fig. 7b. This is not surprising, based on the constraint imposed by the texture and grain shape. However, considering the weak correlation for individual boundaries, the strength of the average correlation shown in Fig. 4 is surprising. Clearly, the point-by-point comparison is a much more rigorous test than the average comparison. It should be noted that the exact grain boundary distribution is probably sensitive to the precise processing parameters.

A previous study showed that the network of grain boundaries in the electrodeposited copper depends on the current characteristics during electrodeposition [68]. Therefore, the pulse forward period and the pulse reverse period could strongly influence the competitive processes of nucleation and grain growth in the electroplated film [69, 70]. During the pulse forward period, the high current density generates a large number of nuclei, which are likely to coalesce. Upon grain coalescence, two abutting grains are zipped together and form a grain boundary. The strain energy induced by the zipping increases the biaxial tensile stress of the electroplated films [71–73]. Recent studies on the in situ stress measurements of copper synthesized by the pulse electroplating showed a significant increase and decrease in the internal stress in every cycle of the pulse on- and pulse off-time periods [74, 75]. The cycle of stress generation and relaxation is similar to a recently suggested grain boundary engineering (GBE) scheme, which uses mechanical cycling at elevated temperature to increase the fraction of Σ3 boundaries in nanocrystalline Ni [76]. According to this approach, it is possible that the formation of the coherent twin boundary in the nanotwinned copper might be similar to the formation mechanism of the annealing twins, which results from the minimization of the interfacial energy and of the elastic strain energy [77, 78]. Because of the limited relaxation during the pulse off- or pulse reverse period, it is likely that the energy is not fully minimized and that residual strains remain in the electroplated nanotwinned copper.

The logarithms of the populations of grain boundaries with Σ3, Σ9, and Σ11 misorientations in the coarse-grained copper in Fig. 7b are correlated to the grain boundary energy with correlation coefficients of −0.89, −0.62, and −0.61, respectively. These correlation factors suggest that the Boltzmann distribution may be applicable to estimate the relative grain boundary population for each misorientation. Before beginning, we note that there is a dramatic change of slope for the high-energy, low population Σ3 boundaries in Fig. 7b. A similar trend between Σ3 grain boundary populations and energies was reported for aluminum, where the interface

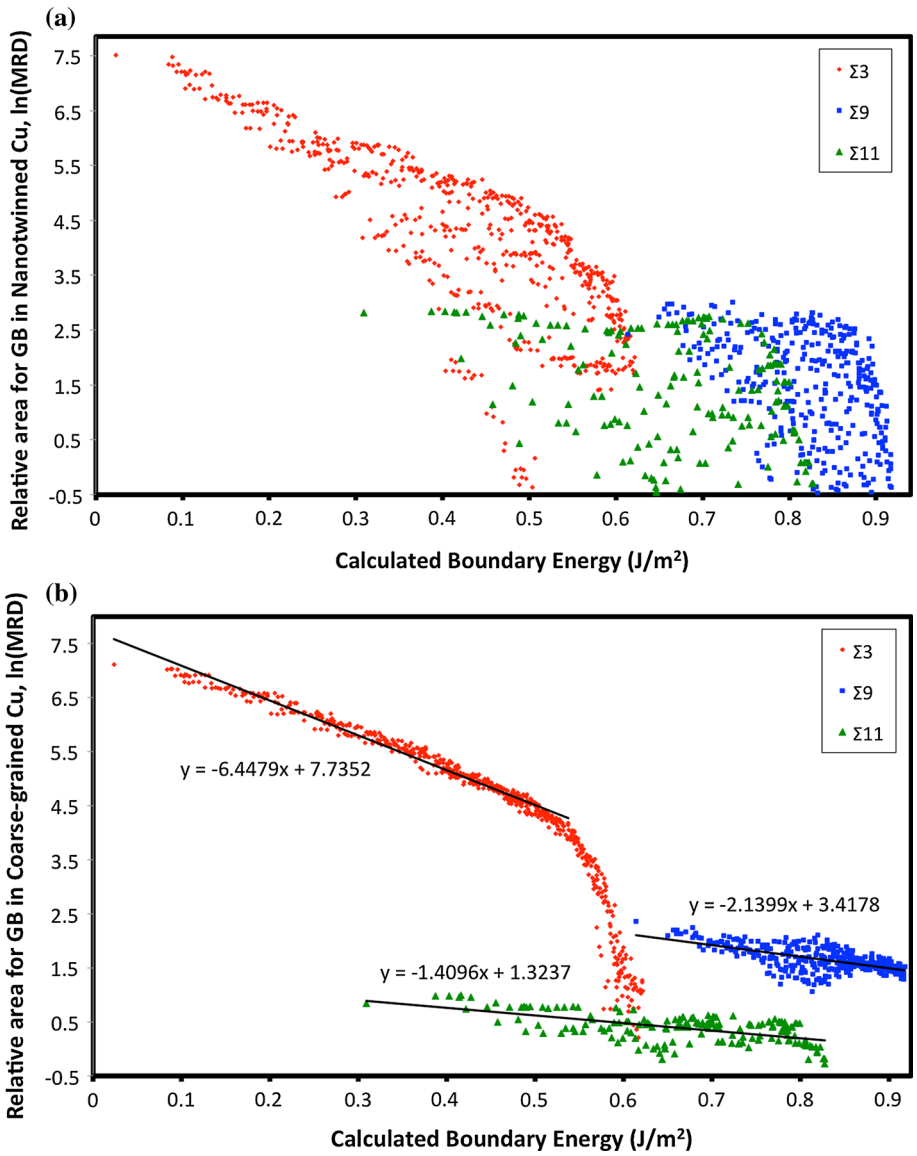

Figure 7 Relationship between grain boundary populations and grain boundary energies in copper for electroplated nanotwinned copper (**a**) and coarse-grained copper (**b**). *Each point* represents a grain boundary type, only Σ3, Σ9, and Σ11 boundaries with populations >0.5 MRD are plotted. The horizontal axis shows the boundary energies, while the vertical axis shows the logarithm of the relative grain boundary areas. The grain boundaries are separated into three categories, Σ3 (*red diamonds*), Σ9 (*blue squares*), and Σ11 (*green triangles*). The trend *lines* for the coarse-grained copper were determined from all data points in the plot at each misorientation, except for Σ3 where only boundaries with a population value above 0.5% of the coherent twin boundary population (1230 MRD) were considered.

populations were also determined stereologically [79], but not for nickel, where the interface populations were determined from 3D data [80]. Therefore, it is possible that the dramatic change in slope for the low population, high-energy boundaries is an artifact of the stereological interpretation of the data, and here we exclude this branch of the curve when calculating the correlation coefficient. Specifically, only such grain boundaries with a relative grain population greater than 0.5% of the coherent twin boundary population were fit to the Boltzmann distribution at Σ3.

Assuming that the energy–population relationship is described by the Boltzmann distribution, the probability of observing a grain boundary with energy (E_i) compared to the total grain boundary population at the Σ3 misorientation ($N^{\Sigma3}_{\text{total}}$) is expressed by

$$P(E_i) = \frac{N(E_i)}{N^{\Sigma3}_{\text{total}}} = \frac{e^{-E_i\alpha_{\Sigma3}/k_B T}}{\xi(\Sigma3, T)}$$
$$N(E_i) = N^{\Sigma3}_{\text{total}} \frac{e^{-E_i\alpha_{\Sigma3}/k_B T}}{\xi(\Sigma3, T)} \quad (1)$$

To render the units correct in this formulation, we introduce $\alpha_{\Sigma3}$ as a unit area variable (m^2) that should scale with the average length of a grain boundary with the Σ3 misorientation. We use k_B for the Boltzmann constant, and T is taken to be experimental temperature (573.5 K). However, the meaning of temperature in this case is not clear, as the events that

alter grain boundary populations are not analogous to the molecular processes usually described by the Boltzmann distribution. The partition function $\xi(\Sigma 3, T)$ is the sum of all energy states (n) at the Σ3 misorientation; $\sum_{i}^{n} e^{-E_i \alpha_{\Sigma 3}/k_B T}$. The logarithm of grain boundary population with E_i is given by

$$\ln N(E_i) = \frac{-E_i \alpha_{\Sigma 3}}{k_B T} + \ln\left(\frac{N_{\text{total}}^{\Sigma 3}}{\xi(\Sigma 3, T)}\right) \quad (2)$$

From Eq. (2), we see that the unit area variable ($\alpha_{\Sigma 3} = 5.1 \times 10^{-20}$ m^2) is determined from the slope of the logarithm of the grain boundary population and the energy of the Σ3 misorientation in Fig. 7b. We find that the unit area variable for Σ11 ($\alpha_{\Sigma 3} = 1.1 \times 10^{-20}$ m^2) is much smaller than $\alpha_{\Sigma 3}$ and slightly smaller than the unit area variable for Σ9 ($\alpha_{\Sigma 9} = 1.7 \times 10^{-20}$ m^2). The fact that the average length of a Σ3 boundary (8 μm) is larger than average lengths of Σ9 (5 μm) or Σ11 (5 μm) boundary suggests that these unit area variables are correlated to the average length for each misorientation. Based on the interpretation of Boltzmann-like distribution, relative grain boundary energies at each misorientation could be derived from relative grain boundary population of annealed polycrystalline copper.

The magnitudes of the unit area variables are also correlated to the grain boundary misorientation distribution. In other words, the larger the average grain boundary population, the greater is the slope of the distribution in Fig. 7b. The grain boundary misorientation distribution can be influenced by the fact that misorientation has to be conserved at the triple junction. According to the sigma combination rule, $\Sigma a \times \Sigma b = m^2 \times \Sigma c$, where Σa, Σb, and Σc are Σ-values of three grain boundaries at the triple junction and m can be any common divisor of Σa and Σb [4]. Because of this, multiple twining ($\Sigma 3^n$) influences the characteristics of triple junctions, the grain boundary misorientation distributions [21, 25, 81, 82], and the relative areas of grain boundaries [30, 83–85]. In the present datasets, the total number fractions of Σ3 boundaries at triple junctions in the nanotwinned copper (38%) and in the coarse-grained copper reference material (49%) are large. If the boundaries are randomly mixed at the triple junctions, the probability of forming a Σ3–Σ3–Σ9 triple junction is square of Σ3 grain boundary fraction, $(\Sigma 3)^2$. The probabilities of forming Σ3–Σ3–Σ9 grain boundaries in the nanotwinned copper (10%) and in the coarse-grained copper (13%) are comparable with the measured concentrations of these junctions (nanotwinned copper = 10% and coarse-grained copper = 16%). Therefore, the Σ3–Σ3–Σ9 junctions in nanotwinned and coarse-grained copper are likely to result from random mixing of the Σ3 boundaries and the crystallographic constraint at the triple junction. The number fractions of Σ3–Σ3–Σ9 junctions are much larger than the length fraction of Σ9 boundaries. This is because the Σ9 boundaries are typically found as short segments in the network connecting Σ3 boundaries. In contrast, Σ3 boundaries typically traverse entire grain diameters or form sinuous structures within grains, so that each Σ3 boundary is much longer than typical Σ9 boundaries. The increase in the population of coherent twins and grain boundaries terminated on {111} planes not only enhances the population of Σ9 grain boundaries but also asymmetric tilt boundaries with <110> misorientations [19, 30, 32].

Our results indicate that while the misorientation specified by the three degrees of freedom is constrained by the geometry of the boundary, the boundary plane distribution is strongly influenced by the grain boundary energy. It should be noted that in the case of coarse-grained copper, a grain boundary can relax to the most energetically favorable grain boundary plane at a fixed misorientation [86–88]. The multiple twining and the geometric constraint at the triple junction significantly influence the topological network and the relative areas of $\Sigma 3^n$ grain boundary in both samples. While there was on average enough grain growth in the electroplated specimen to reach the same distribution as in the coarse-grained specimen, as shown in Fig. 4a, it was not sufficient to achieve to the most energetically favorable grain boundary plane at a fixed misorientation. This results in the significant scatter and a weak correlation between the grain boundary populations and grain boundary energies in Fig. 7a. Therefore, the grain boundary character distribution (GBCD) of nanotwinned copper is thermally unstable and it would be expected to change during high-temperature annealing.

Because electroplating parameters have a significant effect on grain morphology, crystallographic texture, and multiple twining mechanisms [39, 69, 89–96], it is possible to tailor the grain boundary character distribution (GBCD) of electroplated nanotwinned copper by varying voltage,

current density, duty cycle, and the chemistry of the plating bath. It was reported that the crystallographic textures of electroplated copper were changed from [111] to [100] and [101] when the duty cycles of pulsed reverse electrodeposition were reduced [92]. Because the nucleation of nanotwinned lamellae preferentially occurs in the [111] growth direction compared with the [100] and [101] directions [97], electroplated copper having strong [111] texture is expected to have a high density of Σ3 coherent twin boundaries and much finer nanotwinned lamellae. Therefore, electroplated nanotwinned copper with strong [111] texture could be potentially used as interconnects for microelectronic devices because of its excellent mechanical properties, low electrical resistivity, and high electromigration resistance [92, 98, 99]. Recently, it was demonstrated that the nanotwinned lamellae in electroplated copper with strong [111] texture were thermally stable after annealing at 300 °C [100]. While the reason for the thermal stability of the nanotwinned lamellae is not clear, the thermal stability might be related to the grain boundary character distribution (GBCD). It is therefore worth investigating how the GBCD of electroplated nanotwinned copper with strong [111] texture and the grain boundary energy are correlated. Knowledge of the energy population relationship would benefit the design of thermally stable nanocrystalline materials.

Conclusions

The grain boundary character distribution (GBCD) of electroplated nanotwinned copper was compared to the GBCD of a coarse-grained copper reference polycrystal and to grain boundary energies extrapolated from simulated values. While the microstructure of the electroplated nanotwinned copper is much different from the coarse-grained copper, the distribution of relative grain boundary areas for the nanotwinned copper is, on average, comparable to the distribution for coarse-grained copper. We demonstrate that there is a single strong inverse correlation between the grain boundary energy and grain boundary population when groups of boundaries in the same energy range are averaged. When individual boundaries are compared in a point-by-point fashion, a strong inverse correlation is also found, but the slope of the correlation is not the same at all misorientations. In addition to the grain boundary energy, the columnar grain structure, the texture, and the geometric constraints at the triple junctions influenced the grain boundary networks and GBCD of the polycrystalline copper specimens. The findings presented here may enhance the application of grain boundary engineering in electrodeposited copper used in microelectronic interconnect technology.

Acknowledgements

S. Ratanaphan acknowledges the support by the Max-Planck-Gesellschaft Scholarship, the Higher Educational Strategic Scholarship for Frontier Research Network, the Higher Education Research Promotion, and the financial support provided by Research Strengthening Project of the Faculty of Engineering, King Mongkut's University of Technology Thonburi (KMUTT). K. N. Tu acknowledges the support of NSF-Nanoscale Interdisciplinary Research Team Contract CMS-0506841 and thanks Prof. Jianmin Miao and Prof. John H. L. Pang for the copper specimens. The authors thank Dr. S. Zaefferer, B. Sander, S. Igor, A. Katja, and N. Monika for their help with EBSD measurements.

Compliance with ethical standards

Conflict of interest The authors declare that there is no conflict of interest.

References

[1] Rohrer GS, Saylor DM, Dasher BE et al (2004) The distribution of internal interfaces in polycrystals. Z Für Met 95:197–214. doi:10.3139/146.017934

[2] Saylor DM, El-Dasher BS, Adams BL, Rohrer GS (2004) Measuring the five-parameter grain-boundary distribution from observations of planar sections. Metall Mater Trans A 35:1981–1989. doi:10.1007/s11661-004-0147-z

[3] Kim C-S, Rollett AD, Rohrer GS (2006) Grain boundary planes: new dimensions in the grain boundary character distribution. Scr Mater 54:1005–1009. doi:10.1016/j.scriptamat.2005.11.071

[4] Sutton AP, Balluffi RW (1995) Interfaces in crystalline materials. Clarendon, Oxford

[5] Watanabe T (2011) Grain boundary engineering: historical perspective and future prospects. J Mater Sci 46:4095–4115. doi:10.1007/s10853-011-5393-z

[6] Rohrer GS, Randle V (2009) Measurement of the five-parameter grain boundary distribution from planar sections. In: Schwartz AJ, Kumar M, Adams BL, Field DP (eds) Electron backscatter diffraction in materials science. Springer, Berlin, pp 215–229

[7] Zhao Y, Cheng IC, Kassner ME, Hodge AM (2014) The effect of nanotwins on the corrosion behavior of copper. Acta Mater 67:181–188. doi:10.1016/j.actamat.2013.12.030

[8] Lu L, Shen Y, Chen X et al (2004) Ultrahigh strength and high electrical conductivity in copper. Science 304:422–426. doi:10.1126/science.1092905

[9] Xu L, Dixit P, Miao J et al (2007) Through-wafer electroplated copper interconnect with ultrafine grains and high density of nanotwins. Appl Phys Lett 90:033111. doi:10.1063/1.2432284

[10] Zhang X, Wang H, Chen XH et al (2006) High-strength sputter-deposited Cu foils with preferred orientation of nanoscale growth twins. Appl Phys Lett 88:173116. doi:10.1063/1.2198482

[11] Gertsman VY, Bruemmer SM (2001) Study of grain boundary character along intergranular stress corrosion crack paths in austenitic alloys. Acta Mater 49:1589–1598. doi:10.1016/S1359-6454(01)00064-7

[12] Wen YH, Peng HB, Raabe D et al (2014) Large recovery strain in Fe–Mn–Si-based shape memory steels obtained by engineering annealing twin boundaries. Nat Commun 5:4964. doi:10.1038/ncomms5964

[13] Palumbo G, Lehockey EM, Lin P (1998) Applications for grain boundary engineered materials. JOM 50:40–43. doi:10.1007/s11837-998-0248-z

[14] Bieler TR, Eisenlohr P, Roters F et al (2009) The role of heterogeneous deformation on damage nucleation at grain boundaries in single phase metals. Int J Plast 25:1655–1683. doi:10.1016/j.ijplas.2008.09.002

[15] Herbig M, Raabe D, Li YJ et al (2014) Atomic-Scale Quantification of grain boundary segregation in nanocrystalline material. Phys Rev Lett 112:126103. doi:10.1103/PhysRevLett.112.126103

[16] Randle V (2006) "Special" boundaries and grain boundary plane engineering. Scr Mater 54:1011–1015. doi:10.1016/j.scriptamat.2005.11.050

[17] Saylor DM, Morawiec A, Rohrer GS (2003) Distribution of grain boundaries in magnesia as a function of five macroscopic parameters. Acta Mater 51:3663–3674. doi:10.1016/S1359-6454(03)00181-2

[18] Ratanaphan S, Olmsted DL, Bulatov VV et al (2015) Grain boundary energies in body-centered cubic metals. Acta Mater 88:346–354. doi:10.1016/j.actamat.2015.01.069

[19] Randle V (2010) Role of grain boundary plane in grain boundary engineering. Mater Sci Technol 26:774–780. doi:10.1179/026708309X12567268926641

[20] Saylor DM, El Dasher BS, Rollett AD, Rohrer GS (2004) Distribution of grain boundaries in aluminum as a function of five macroscopic parameters. Acta Mater 52:3649–3655. doi:10.1016/j.actamat.2004.04.018

[21] Randle V (2004) Twinning-related grain boundary engineering. Acta Mater 52:4067–4081. doi:10.1016/j.actamat.2004.05.031

[22] Watanabe T (1984) An approach to grain boundary design of strong and ductile polycrystals. Res Mech 11:47–84

[23] Raabe D, Sandlöbes S, Millán J et al (2013) Segregation engineering enables nanoscale martensite to austenite phase transformation at grain boundaries: a pathway to ductile martensite. Acta Mater 61:6132–6152. doi:10.1016/j.actamat.2013.06.055

[24] Gertsman VY, Janecek M, Tangri K (1996) Grain boundary ensembles in polycrystals. Acta Mater 44:2869–2882. doi:10.1016/1359-6454(95)00396-7

[25] Randle V (1999) Mechanism of twinning-induced grain boundary engineering in low stacking-fault energy materials. Acta Mater 47:4187–4196. doi:10.1016/S1359-6454(99)00277-3

[26] Kumar M, Schwartz AJ, King WE (2002) Microstructural evolution during grain boundary engineering of low to medium stacking fault energy fcc materials. Acta Mater 50:2599–2612. doi:10.1016/S1359-6454(02)00090-3

[27] Winning M (2007) Grain boundary mechanics. Cuvillier Verlag, Göttingen

[28] Randle V, Rohrer GS, Miller HM et al (2008) Five-parameter grain boundary distribution of commercially grain boundary engineered nickel and copper. Acta Mater 56:2363–2373. doi:10.1016/j.actamat.2008.01.039

[29] Saylor DM, El Dasher B, Pang Y et al (2004) Habits of grains in dense polycrystalline solids. J Am Ceram Soc 87:724–726. doi:10.1111/j.1551-2916.2004.00724.x

[30] Kim C-S, Hu Y, Rohrer GS, Randle V (2005) Five-parameter grain boundary distribution in grain boundary engineered brass. Scr Mater 52:633–637. doi:10.1016/j.scriptamat.2004.11.025

[31] Randle V, Hu Y, Rohrer GS, Kim C-S (2005) Distribution of misorientations and grain boundary planes in grain boundary engineered brass. Mater Sci Technol 21:1287–1292. doi:10.1179/174328405X66996

[32] Rohrer GS, Randle V, Kim C-S, Hu Y (2006) Changes in the five-parameter grain boundary character distribution in α-brass brought about by iterative thermomechanical processing. Acta Mater 54:4489–4502. doi:10.1016/j.actamat.2006.05.035

[33] Randle V, Jones R (2009) Grain boundary plane distributions and single-step versus multiple-step grain boundary engineering. Mater Sci Eng A 524:134–142. doi:10.1016/j.msea.2009.06.018

[34] Jones R, Randle V, Engelberg D, Marrow TJ (2009) Five-parameter grain boundary analysis of a grain boundary–engineered austenitic stainless steel. J Microsc 233:417–422. doi:10.1111/j.1365-2818.2009.03129.x

[35] Chen K-C, Wu W-W, Liao C-N et al (2008) Observation of atomic diffusion at twin-modified grain boundaries in copper. Science 321:1066–1069. doi:10.1126/science.1160777

[36] Dixit P, Xu L, Miao J et al (2007) Mechanical and microstructural characterization of high aspect ratio through-wafer electroplated copper interconnects. J Micromech Microeng 17:1749–1757. doi:10.1088/0960-1317/17/9/001

[37] Zhong S, Koch T, Wang M et al (2009) Nanoscale twinned copper nanowire formation by direct electrodeposition. Small 5:2265–2270. doi:10.1002/smll.200900746

[38] Hodge AM, Wang YM, Barbee TW Jr (2008) Mechanical deformation of high-purity sputter-deposited nano-twinned copper. Scr Mater 59:163–166. doi:10.1016/j.scriptamat.2008.02.048

[39] Hsiao H-Y, Liu C-M, Lin H et al (2012) Unidirectional growth of microbumps on (111)-oriented and nanotwinned copper. Science 336:1007–1010. doi:10.1126/science.1216511

[40] Khorashadizadeh A, Raabe D, Zaefferer S et al (2011) Five-parameter grain boundary analysis by 3D EBSD of an ultra fine grained CuZr alloy processed by equal channel angular pressing. Adv Eng Mater 13:237–244. doi:10.1002/adem.201000259

[41] Khorashadizadeh A, Winning M, Raabe D (2008) 3D tomographic EBSD measurements of heavily deformed ultra fine grained Cu-0.17 wt%Zr obtained from ECAP. Mater Sci Forum 584–586:434–439. doi:10.4028/www.scientific.net/MSF.584-586.434

[42] Mandal S, Pradeep KG, Zaefferer S, Raabe D (2014) A novel approach to measure grain boundary segregation in bulk polycrystalline materials in dependence of the boundaries' five rotational degrees of freedom. Scr Mater 81:16–19. doi:10.1016/j.scriptamat.2014.02.016

[43] Saylor DM, Morawiec A, Rohrer GS (2002) Distribution and energies of grain boundaries in magnesia as a function of five degrees of freedom. J Am Ceram Soc 85:3081–3083. doi:10.1111/j.1151-2916.2002.tb00583.x

[44] Li J, Dillon SJ, Rohrer GS (2009) Relative grain boundary area and energy distributions in nickel. Acta Mater 57:4304–4311. doi:10.1016/j.actamat.2009.06.004

[45] Rohrer GS (2011) Grain boundary energy anisotropy: a review. J Mater Sci 46:5881–5895. doi:10.1007/s10853-011-5677-3

[46] Rohrer GS (2011) Measuring and interpreting the structure of grain-boundary networks. J Am Ceram Soc 94:633–646. doi:10.1111/j.1551-2916.2011.04384.x

[47] Beladi H, Rohrer GS (2013) The relative grain boundary area and energy distributions in a ferritic steel determined from three-dimensional electron backscatter diffraction maps. Acta Mater 61:1404–1412. doi:10.1016/j.actamat.2012.11.017

[48] Beladi H, Nuhfer NT, Rohrer GS (2014) The five-parameter grain boundary character and energy distributions of a fully austenitic high-manganese steel using three dimensional data. Acta Mater 70:281–289. doi:10.1016/j.actamat.2014.02.038

[49] Ratanaphan S, Boonkird T, Sarochawikasit R et al (2017) Atomistic simulations of grain boundary energies in tungsten. Mater Lett 186:116–118. doi:10.1016/j.matlet.2016.09.104

[50] Liu X, Choi D, Beladi H et al (2013) The five-parameter grain boundary character distribution of nanocrystalline tungsten. Scr Mater 69:413–416. doi:10.1016/j.scriptamat.2013.05.046

[51] Gruber J, George DC, Kuprat AP et al (2005) Effect of anisotropic grain boundary properties on grain boundary plane distributions during grain growth. Scr Mater 53:351–355. doi:10.1016/j.scriptamat.2005.04.004

[52] Dillon SJ, Rohrer GS (2009) Mechanism for the development of anisotropic grain boundary character distributions during normal grain growth. Acta Mater 57:1–7. doi:10.1016/j.actamat.2008.08.062

[53] Holm EA, Olmsted DL, Foiles SM (2010) Comparing grain boundary energies in face-centered cubic metals: Al, Au, Cu and Ni. Scr Mater 63:905–908. doi:10.1016/j.scriptamat.2010.06.040

[54] Bulatov VV, Reed BW, Kumar M (2014) Grain boundary energy function for fcc metals. Acta Mater 65:161–175. doi:10.1016/j.actamat.2013.10.057

[55] Dixit P, Miao J (2006) Aspect-ratio-dependent copper electrodeposition technique for very high aspect-ratio through-hole plating. J Electrochem Soc 153:G552–G559. doi:10.1149/1.2189238

[56] Wright SI, Larsen RJ (2002) Extracting twins from orientation imaging microscopy scan data. J Microsc 205:245–252. doi:10.1046/j.1365-2818.2002.00992.x

[57] Ratanaphan S (2013) Grain boundary character distributions in isostructural materials. Carnegie Mellon University, Pittsburgh

[58] Olmsted DL (unpublished)

[59] Olmsted DL, Foiles SM, Holm EA (2009) Survey of computed grain boundary properties in face-centered cubic

metals: I. Grain boundary energy. Acta Mater 57:3694–3703. doi:10.1016/j.actamat.2009.04.007

[60] Duggan BJ, Lücke K, Köhlhoff G, Lee CS (1993) On the origin of cube texture in copper. Acta Metall Mater 41:1921–1927. doi:10.1016/0956-7151(93)90211-A

[61] Ridha AA, Hutchinson WB (1982) Recrystallisation mechanisms and the origin of cube texture in copper. Acta Metall 30:1929–1939. doi:10.1016/0001-6160(82)90033-5

[62] Mackenzie JK, Moore AJW, Nicholas JF (1962) Bonds broken at atomically flat crystal surfaces—I. J Phys Chem Solids 23:185–196. doi:10.1016/0022-3697(62)90001-X

[63] McLean M (1971) Determination of the surface energy of copper as a function of crystallographic orientation and temperature. Acta Metall 19:387–393. doi:10.1016/0001-6160(71)90106-4

[64] Zhang J-M, Ma F, Xu K-W (2004) Calculation of the surface energy of FCC metals with modified embedded-atom method. Appl Surf Sci 229:34–42. doi:10.1016/j.apsusc.2003.09.050

[65] Wolf D, Yip S (1992) Materials interfaces—atomic-level structure and properties. Springer, Berlin

[66] Ratanaphan S, Yoon Y, Rohrer GS (2014) The five parameter grain boundary character distribution of polycrystalline silicon. J Mater Sci 49:4938–4945. doi:10.1007/s10853-014-8195-2

[67] Brandon DG (1966) The structure of high-angle grain boundaries. Acta Metall 14:1479–1484. doi:10.1016/0001-6160(66)90168-4

[68] Liu T-C, Liu C-M, Huang Y-S et al (2013) Eliminate Kirkendall voids in solder reactions on nanotwinned copper. Scr Mater 68:241–244. doi:10.1016/j.scriptamat.2012.10.024

[69] Natter H, Hempelmann R (1996) Nanocrystalline copper by pulsed electrodeposition: the effects of organic additives, bath temperature, and pH. J Phys Chem 100:19525–19532. doi:10.1021/jp9617837

[70] Natter H, Hempelmann R (2003) Tailor-made nanomaterials designed by electrochemical methods. Electrochim Acta 49:51–61. doi:10.1016/j.electacta.2003.04.004

[71] Hoffman R (1976) Stresses in thin films: the relevance of grain boundaries and impurities. Thin Solid Films 34:185–190. doi:10.1016/0040-6090(76)90453-3

[72] Nix WD, Clemens BM (1999) Crystallite coalescence: a mechanism for intrinsic tensile stresses in thin films. J Mater Res 14:3467–3473. doi:10.1557/JMR.1999.0468

[73] Chaudhari P (1972) Grain growth and stress relief in thin films. J Vac Sci Technol 9:520–522. doi:10.1116/1.1316674

[74] Xu D, Sriram V, Ozolins V et al (2009) In situ measurements of stress evolution for nanotwin formation during pulse electrodeposition of copper. J Appl Phys 105:023521. doi:10.1063/1.3068191

[75] Xu D, Sriram V, Ozolins V et al (2008) Nanotwin formation and its physical properties and effect on reliability of copper interconnects. Microelectron Eng 85:2155–2158. doi:10.1016/j.mee.2008.04.035

[76] Bober DB, Kumar M, Rupert TJ (2015) Nanocrystalline grain boundary engineering: increasing Σ3 boundary fraction in pure Ni with thermomechanical treatments. Acta Mater 86:43–54. doi:10.1016/j.actamat.2014.11.034

[77] Xu D, Kwan WL, Chen K et al (2007) Nanotwin formation in copper thin films by stress/strain relaxation in pulse electrodeposition. Appl Phys Lett 91:254105. doi:10.1063/1.2825412

[78] Fullman RL, Fisher JC (1951) Formation of annealing twins during grain growth. J Appl Phys 22:1350–1355. doi:10.1063/1.1699865

[79] Holm EA, Rohrer GS, Foiles SM et al (2011) Validating computed grain boundary energies in fcc metals using the grain boundary character distribution. Acta Mater 59:5250–5256. doi:10.1016/j.actamat.2011.05.001

[80] Rohrer GS, Holm EA, Rollett AD et al (2010) Comparing calculated and measured grain boundary energies in nickel. Acta Mater 58:5063–5069. doi:10.1016/j.actamat.2010.05.042

[81] Miyazawa K, Iwasaki Y, Ito K, Ishida Y (1996) Combination rule of Σ values at triple junctions in cubic polycrystals. Acta Crystallogr A 52:787–796. doi:10.1107/S0108767396005934

[82] Gertsman VY, Tangri K (1995) Computer simulation study of grain boundary and triple junction distributions in microstructures formed by multiple twinning. Acta Metall Mater 43:2317–2324. doi:10.1016/0956-7151(94)00422-6

[83] Schuh CA, Kumar M, King WE (2005) Universal features of grain boundary networks in FCC materials. J Mater Sci 40:847–852. doi:10.1007/s10853-005-6500-9

[84] Minich RW, Schuh CA, Kumar M (2002) Role of topological constraints on the statistical properties of grain boundary networks. Phys Rev B 66:052101. doi:10.1103/PhysRevB.66.052101

[85] Rohrer GS, Miller HM (2010) Topological characteristics of plane sections of polycrystals. Acta Mater 58:3805–3814. doi:10.1016/j.actamat.2010.03.028

[86] Randle V, Hu Y, Coleman M (2008) Grain boundary reorientation in copper. J Mater Sci 43:3782–3791. doi:10.1007/s10853-007-2128-2

[87] Lejček P, Šedá P, Kinoshita Y et al (2012) Grain boundary plane reorientation: model experiments on bi- and tricrystals. J Mater Sci 47:5106–5113. doi:10.1007/s10853-012-6384-4

[88] Dunn CG, Lionetti F (1949) The effect of orientation difference on grain boundary energies. Trans Am Inst Min Metall Eng 185:125–132

[89] Schlesinger M, Paunovic M (2011) Modern electroplating. Wiley, New York

[90] Bicelli LP, Bozzini B, Mele C (2008) A review of nanostructural aspects of metal electrodeposition. Int J Electrochem Sci 3:356–408

[91] Chandrasekar MS, Pushpavanam M (2008) Pulse and pulse reverse plating—conceptual, advantages and applications. Electrochim Acta 53:3313–3322. doi:10.1016/j.electacta.2007.11.054

[92] Pavithra CLP, Sarada BV, Rajulapati KV et al (2015) Controllable crystallographic texture in copper foils exhibiting enhanced mechanical and electrical properties by pulse reverse electrodeposition. Cryst Growth Des 15:4448–4458. doi:10.1021/acs.cgd.5b00748

[93] Liu T-C, Liu C-M, Hsiao H-Y et al (2012) Fabrication and characterization of (111)-oriented and nanotwinned Cu by Dc electrodeposition. Cryst Growth Des 12:5012–5016. doi:10.1021/cg300962v

[94] Chan T-C, Chueh Y-L, Liao C-N (2011) Manipulating the crystallographic texture of nanotwinned Cu films by electrodeposition. Cryst Growth Des 11:4970–4974. doi:10.1021/cg200877f

[95] Liu C-M, Lin H-W, Lu C-L, Chen C (2014) Effect of grain orientations of Cu seed layers on the growth of <111>-oriented nanotwinned Cu. Sci Rep 4:6123. doi:10.1038/srep06123

[96] Hasegawa M, Mieszala M, Zhang Y et al (2015) Orientation-controlled nanotwinned copper prepared by electrodeposition. Electrochim Acta 178:458–467. doi:10.1016/j.electacta.2015.08.022

[97] Zhou XW, Wadley HNG (1999) Twin formation during the atomic deposition of copper. Acta Mater 47:1063–1078. doi:10.1016/S1359-6454(98)00403-0

[98] Ryu C, Kwon K-W, Loke ALS et al (1999) Microstructure and reliability of copper interconnects. IEEE Trans Electron Devices 46:1113–1120. doi:10.1109/16.766872

[99] Sarada BV, Pavithra CLP, Ramakrishna M et al (2010) Highly (111) textured copper foils with high hardness and high electrical conductivity by pulse reverse electrodeposition. Electrochem Solid-State Lett 13:D40–D42. doi:10.1149/1.3358145

[100] Huang Y-S, Liu C-M, Chiu W-L, Chen C (2014) Grain growth in electroplated (1 1 1)-oriented nanotwinned Cu. Scr Mater 89:5–8. doi:10.1016/j.scriptamat.2014.06.008